Automatically Determining the Confocal Parameters From OCT B-Scans for Quantification of the Attenuation Coefficients

Nicholas Dwork, Gennifer T. Smith, Theodore Leng, John M. Pauly, and Audrey K. Bowden

***Abstract*— The attenuation coefficient is a relevant biomarker for many diagnostic medical applications. Recently, the Depth-Resolved Confocal (DRC) technique was developed to automatically estimate the attenuation coefficients from Optical Coherence Tomography (OCT) data with pixel-level resolution. However, DRC requires that the confocal function parameters (i.e., focal plane location and apparent Rayleigh range) be known *a priori*. In this paper, we present the autoConfocal algorithm: a simple, automatic method for estimating those parameters directly from OCT imagery when the focal plane is within the sample. We present autoConfocal+DRC results on phantom data, *ex-vivo* biological tissue data, and *in-vivo* clinical data.**

***Index Terms*— Optical coherence tomography, attenuation coefficient, confocal function, optimization.**

I. Introduction

OPTICAL Coherence Tomography (OCT) is a high-resolution imaging modality that is gaining popularity in ophthalmology, dermatology, cardiology, and urology. The quantification of relevant physical parameters, such as those that can be extracted from OCT data, has been shown to be important for disease diagnosis and cancer staging in many imaging modalities [1]–[3]. For example, quantification of the attenuation coefficient, which characterizes the rate of change of the OCT signal as a function of depth, has been shown to be relevant for differentiating tissue type in the lumen vessel [4], glaucoma diagnosis [5], renal tumor differentiation [6], bladder cancer staging [7], and brain cancer detection [8], [9].

In their seminal work, Vermeer *et al.* [10] introduced the Depth-Resolved (DR) algorithm to automatically estimate the attenuation coefficient for each pixel of an OCT image. DR requires the focal plane be placed high above the sample to yield accurate results. In this regime, the confocal function is approximately constant throughout the field of view, which simplifies the processing. Unfortunately, this restriction reduces the signal-to-noise ratio (SNR) and is impractical for certain clinical applications. Van Leeuwen *et al.* [11] demonstrated that the attenuation coefficients can be accurately estimated when the focal plane is located within the sample if the confocal function is taken into account. Smith *et al.* [12] introduced a modification of DR, called Depth-Resolved Confocal (DRC), to automatically quantify the attenuation coefficient at each pixel even when the focal plane is located within the sample. A disadvantage of DRC, however, is that it requires *a priori* knowledge of the confocal function parameters of the OCT system employed (i.e., the focal plane depth and the apparent Rayleigh range).

Both Van Leeuwen *et al.* [11] and Almasian *et al.* [13] have presented methods for calculating the confocal function parameters by imaging a mirror or weakly scattering medium of constant attenuation, respectively. These methods would require a technician to image a separate sample prior to imaging the patient, which could be cumbersome in a clinical setting. With ophthalmic imaging, the eye is part of the imaging system and would need to be included in any calibration scan. Lastly, some OCT imaging applications require that a probe be sterile prior to imaging the subject (e.g., intravascular imaging [14], [15] and bladder imaging [16], [17]), which prohibits imaging of a separate sample prior to the clinical scan; after the clinical scan, the probe may be damaged or dirty. Thus, it would be beneficial to have a method of calibration that can be performed during the clinical scan itself.

This work presents a simple, fast, and automatic technique for extracting the confocal function parameters of a system from the imagery itself when the focal plane is close

Manuscript received June 13, 2018; revised July 20, 2018; accepted July 24, 2018. Date of publication July 31, 2018; date of current version December 28, 2018. The work of N. Dwork was supported in part by the Gerald J. Lieberman Fellowship, in part by the National Institute of Health's—Predoctoral Training in Biomedical Imaging at Stanford University under Grant T32EB009653, in part by The Rose Hills Foundation Graduate Engineering Fellowship, in part by The Electrical Engineering Department New Projects Graduate Fellowship, and in part by The Oswald G. Villard Jr. Engineering Fellowship. The work of G. T. Smith was supported in part by an NSFGRFP Fellowship and in part by an ARCS Foundation Scholar Award. *(Nicholas Dwork and Gennifer T. Smith contributed equally to this work.) (Corresponding author: Audrey Bowden.)*

N. Dwork, G. T. Smith, J. M. Pauly, and A. K. Bowden are with the Department of Electrical Engineering, Stanford University, Stanford, CA 94305 USA (e-mail: audrey@ee.stanford.edu).

T. Leng is with the Department of Ophthamology, Stanford University Medical Center, Stanford, CA 94305 USA.

This paper has supplementary downloadable material available at http://ieeexplore.ieee.org, provided by the author.

Color versions of one or more of the figures in this paper are available online at http://ieeexplore.ieee.org.

Digital Object Identifier 10.1109/TMI.2018.2861570

to or within the sample; we call this technique autoConfocal.[1] In brief, the effect of the confocal function can be visualized, and therefore extracted, by observing the difference between two images of the same object captured by the same imaging system with slightly different views. The change in relative contrast of features stems from the confocal function and may be extracted through image processing techniques. When combined with a suitable technique for estimating the attenuation coefficient, autoConfocal enables automated, accurate estimation of the attenuation coefficient in OCT systems even when the focal plane is located within the sample.[2]

II. Signal Model

In this section, we summarize the OCT signal model.[3] The intensity at each depth z of an A-scan may be modeled as

$$I_f(z) = h(z)\, f(z)\, \beta\, r(z)\, \exp\left(-2\int_0^z \mu(\epsilon)\, d\epsilon\right), \tag{1}$$

where f models the fall-off effect [19], [20], β is a constant of proportionality (which accounts for the quantum efficiency of the detector, the coherence length, the size of the detector, and the intensity of the light source), $r(z)$ is the fraction of attenuated light that is backscattered, $\mu(z)$ is the attenuation coefficient due to scattering, and ϵ is a variable of integration [10]. The function h is the confocal function:

$$h(z) = \left(\left(\frac{z - z_0}{z_R}\right)^2 + 1\right)^{-1}, \tag{2}$$

where $z_0 \in \mathbb{R}$ is the focal plane depth and z_R is the apparent Rayleigh range defined as

$$z_R = \alpha\, n\, z_r. \tag{3}$$

The variable n represents the index of refraction of the sample, z_r is the Rayleigh range, and $\alpha = 2$ for diffuse samples.

The signal vector $\boldsymbol{I}_f^{(c)} \in \mathbb{R}^M$ is

$$\boldsymbol{I}_f^{(c)}[m] = \int_{z_m}^{z_{m+1}} I_f(z)\, dz + \boldsymbol{c}[m], \tag{4}$$

where z_m and z_{m+1} are the bounds on the m^{th} pixel, and $\boldsymbol{c}$ is an independent identically distributed random vector.

III. Methods

A. Estimating the Confocal Function Parameters

In order for DRC to estimate the depth-dependent attenuation coefficients, the confocal function h must be known. It can be seen in (1) that if the attenuation coefficients μ are unknown then there is insufficient information to determine h from a single scan. However, by leveraging the common information present in two B-scans that image overlapping regions of the same sample, estimates of z_0 and z_R can be obtained. This fact underlies the general strategy we implement in this work.

The goal is to find a function of two de-speckled B-scans – $\boldsymbol{I}_{f,1}^{(c)}$ and $\boldsymbol{I}_{f,2}^{(c)}$ – that is solely dependent on the confocal function parameters z_0 and z_R. Image processing can determine approximations for the mean and variance of the noise $\boldsymbol{c}$ (refer to §III-C). Once the mean of the noise is estimated ($\hat{\bar{c}}$), the noise bias is removed from both B-scans as follows: $\hat{\boldsymbol{I}}_{f,j} = \boldsymbol{I}_{f,j}^{(c)} - \hat{\bar{c}}$, where $\hat{}$ denotes an estimated value. Once de-biased, a Hadamard division accounts for fall-off: $\hat{\boldsymbol{I}}_{\boldsymbol{j}} = \hat{\boldsymbol{I}}_{f,j} \oslash \boldsymbol{f}$, where $\boldsymbol{f}$ is a vector of fall-off function values corresponding to the depths of each pixel in the A-scan [10].

Consider two de-speckled and de-biased OCT B-scans ($\hat{\boldsymbol{I}}_{\boldsymbol{1}}$ and $\hat{\boldsymbol{I}}_{\boldsymbol{2}}$) with overlapping image content for which the underlying samples are related by a rotation and a translation. The underlying attenuation coefficient functions $\mu_1, \mu_2 : \mathbb{R}^2 \to \mathbb{R}$ are related by $\mu_1(p) = \mu_2\left(\mathcal{T}_{\Delta x, \Delta z}\, \mathcal{R}_\theta\, p\right)$, where $p \in \mathbb{R}^2$. The operator $\mathcal{R}_\theta$ is a rotation of angle θ, and $\mathcal{T}_{\Delta x, \Delta z}$ is a translation of Δx laterally and Δz axially. If the images are captured by Spectral Domain OCT (SD-OCT), it is further assumed that the relevant structure in both images fits within the Nyquist-limited ranging depth of the system.

If the rotation angle θ is small (less than 20°), the rotation can be approximated by a vertical shear [21]. By doing so, the confocal function remains a longitudinal effect after the shear. Thus, we make the approximation that $\mu_1(p) \approx \mu_2\left(\mathcal{T}_{\Delta x, \Delta z}\, \mathcal{S}_\theta\, p\right)$, where $\mathcal{S}_\theta$ is a vertical shear of angle θ:

$$\mathcal{S}_\theta\, p = \begin{bmatrix} 1 & 0 \\ \tan(\theta) & 1 \end{bmatrix} \begin{bmatrix} x \\ z \end{bmatrix},$$

and x and z are the lateral and axial components of p.

Image processing can determine the vertical shear and translation that relate the B-scans (refer to §III-C). Let n and m be the indices for a pixel in a B-scan in the lateral and axial directions, respectively. Then $n = x\, s_x$ and $m = z\, s_z$ where s_x and s_z are the lateral and axial pixel sizes (in μm). Once the transformations have been determined, the images can be aligned by calculating $\hat{\boldsymbol{I}}_2\left(n', m'\right)$, where

$$\begin{bmatrix} n' \\ m' \end{bmatrix} = \begin{bmatrix} s_x & 0 \\ 0 & s_z \end{bmatrix} \mathcal{T}_{\Delta x, \Delta z}\, \mathcal{S}_\theta\, p.$$

After alignment, $\hat{\boldsymbol{I}}_1(n, m)$ and $\hat{\boldsymbol{I}}_2\left(n', m'\right)$ represent the same location. Since n' and m' are not generally integers, the value of $\hat{\boldsymbol{I}}_2\left(n', m'\right)$ must be determined through interpolation.

After alignment, almost all the parameters of (1) are the same; the only difference is the location of the focal plane. This redundancy theoretically permits the use of the following expression to isolate the parameters of the confocal function:

$$\frac{\hat{\boldsymbol{I}}_1(n, m)}{\hat{\boldsymbol{I}}_2(n', m')} = \frac{\left(\frac{z + \Delta z + Z_n - z_0}{z_R}\right)^2 + 1}{\left(\frac{z - z_0}{z_R}\right)^2 + 1}, \tag{5}$$

where $Z_n = \tan(\theta)\, x$ is the longitudinal displacement of the n^{th} A-scan due to the vertical shear, and z is the depth corresponding to index m.

Rather than working in intensity values, we convert the values of $\hat{\boldsymbol{I}}$ to decibels (dB), the standard unit for presenting OCT data: $\hat{\boldsymbol{I}}^{(\text{dB})} = 10 \log_{10}\left(\hat{\boldsymbol{I}}\right)$. After the conversion, (5)

[1] The techniques presented in this paper are an extension of the work previously presented in [18].

[2] Appendices for this manuscript are located in the supplemental document, which is available online in the supplementary files /multimedia tab.

[3] Details of the signal model can be found in Appendix A.

becomes a subtraction:

$$\hat{\boldsymbol{I}}_1^{(dB)}(n,m) - \hat{\boldsymbol{I}}_2^{(dB)}(n',m') = 10\log_{10}\left(\left(\frac{z+\Delta z+Z_n-z_0}{z_R}\right)^2+1\right) - 10\log_{10}\left(\left(\frac{z-z_0}{z_R}\right)^2+1\right).$$

The following related problem is solved to find z_0 and z_R:

$$\underset{z_0,z_R}{\text{minimize}} \left\| \left[\hat{\boldsymbol{I}_1}^{(dB)}(n,m) - \hat{\boldsymbol{I}_2}^{(dB)}(n',m')\right] - \left[10\log_{10}\left(\left(\frac{z+\Delta z+Z_n-z_0}{z_R}\right)^2+1\right) - 10\log_{10}\left(\left(\frac{z-z_0}{z_R}\right)^2+1\right)\right] \right\|_{w,1} \quad \text{subject to } z_R > 0, \tag{6}$$

where $\|\cdot\|_{w,1}$ represents the weighted L_1 norm (defined as $\|x\|_{w,1} = \sum_i w_i |x_i|$, where $w_i > 0$ for all i).

Differences between the data and model occur where the rotation does not approximate a vertical shear well (e.g., at vertical edges) or where the SNR is low. The L_1 norm in (6) is robust against these outliers [22]. The weights are set according to $w(n,m) = \max\left(0, \min\left(\hat{\boldsymbol{I}_1}^{(dB)}(n,m), \hat{\boldsymbol{I}_2}^{(dB)}(n',m')\right)\right)$ so that pixels with higher SNR in both images contribute more to the final estimate.

B. Estimation and Error of the Attenuation Coefficients

Once the confocal function's parameters have been determined with autoConfocal, the attenuation coefficients can be estimated using DRC [12] (as summarized in Appendix B). Here, we follow a derivation similar to that in [10] to develop an understanding of the error associated with this technique.

After accounting for the confocal function and fall-off, the signal model of (1) becomes

$$I(z) = \beta\, r(z)\, \exp\left(-2\int_0^z \mu(\epsilon)\, d\epsilon\right). \tag{7}$$

We make the approximation that the amount of backscattered light is proportional to the total amount of scattered light: $r(z) = \nu\, \mu_s(z)$, where $\nu \geq 0$. Note this is a different approximation than that used by Vermeer et al. to develop DR, wherein the reflectivity was assumed proportional to the full attenuation coefficient (which is the sum of the attenuation due to scattering and due to absorption): $\mu = \mu_s + \mu_a$. The DRC model of (7) can be expressed as follows:

$$I(z) = \bar{\beta}\, (\mu(z) - \mu_a(z))\, \exp\left(-2\int_0^s \mu(\epsilon)\, d\epsilon\right),$$

where $\bar{\beta} = \nu\beta$. Integrating from depth z to the final imaging depth D,

$$\int_z^D I(s)\, ds = \frac{-\bar{\beta}}{2}\exp\left(-2\int_0^s \mu(\epsilon)\, d\epsilon\right)\Big|_z^D - \bar{\beta}\int_z^D \mu_a(s)\exp\left(-2\int_0^s \mu(\epsilon)\, d\epsilon\right) ds.$$

We assume further (as was done in [10]) that the intensity of light that reaches depth D is negligible. Therefore,

$$\int_z^D I(s)\, ds = \frac{\nu\, I(z)}{2\, r(z)} - \bar{\beta}\int_z^D \mu_a(s)\exp\left(-2\int_0^s \mu(\epsilon)\, d\epsilon\right) ds.$$

Rearranging terms yields

$$\mu_s(z)\,(1+E(z)) = \frac{I(z)}{2\int_z^D I(s)\, ds}, \tag{8}$$

where the error factor E is

$$E(z) = \frac{\int_z^D \frac{\mu_a(s)}{\mu_s(s)} I(s)\, ds}{\int_z^D I(s)\, ds} \tag{9}$$

$$\leq \max\left(\left\{\frac{\mu_a(s)}{\mu_s(s)} : s \in [z, D]\right\}\right). \tag{10}$$

Equation (8) shows that DRC estimates the scattering coefficient, which is nearly equal to the attenuation coefficient when absorption is negligible. Eq. (9) shows that the error at depth z (excluding numerical residuals) is equal to a weighted average of μ_a/μ_s over the interval $[z, D]$. It is bounded above by the maximum of μ_a/μ_s, as shown in (10). After approximating the integration of (8) with a Riemann sum, we arrive at the DR algorithm of [10].

C. Algorithm Implementation

The autoConfocal algorithm is an adjunct set of processing steps to the DRC algorithm; together, they permit an automatic estimation of the attenuation coefficient of each pixel of a B-scan without *a priori* knowledge of the confocal function. The outputs of autoConfocal (the confocal function parameters z_0 and z_R) are input directly into DRC, which estimates the attenuation coefficients. Fig. 1 and Alg. 1 summarize the autoConfocal and DRC algorithms. The inputs are two processed B-scans (each composed of N A-scans and M rows) that are related by a translation and possibly a small rotation. The output is an $M \times N$ image (or 2D array) where the value of each pixel is the corresponding attenuation coefficient. A detailed description of each step of the algorithm follows.

Algorithm 1 AutoConfocal+DRC

Inputs: B-scans 1 and 2
Step 1 Clean data and convert to decibels
Step 2 Filter converted B-scans
Step 3 Align filtered B-scans
Step 4 Determine the parameters of the confocal function: z_0 and z_R
Step 5 Use DRC to estimate the attenuation coefficient of each pixel in B-scan 1

Step 1 (Clean the Data and Convert to Decibels): Input two intensity B-scans. Denote the minimum values of the two B-scans as m_1 and m_2, respectively. For each B-scan, use the median of the top 5% of rows (which is assumed to contain no sample structure) as an estimate of the mean of the additive noise sources [23]; denote these values as $\hat{\bar{c}}_1$ and $\hat{\bar{c}}_2$ in B-scan 1 and 2, respectively. To improve

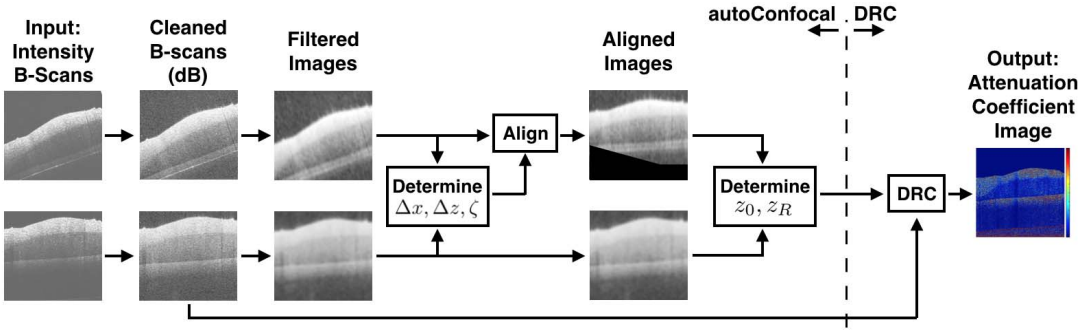

Fig. 1. Summary of the autoConfocal+DRC algorithm, which automatically determines the confocal function parameters (z_0 and z_R) and estimates the attenuation coefficient of each pixel of a B-scan.

accuracy while maintaining precision, de-bias the data by setting the value of each pixel in the i^{th} B-scan according to $\hat{\boldsymbol{I}}_{f,i}(p) = \max\left(\boldsymbol{I}_{f,i}^{(c)}(p) - \hat{\bar{c}}_i, m_i\right)$. The maximum operation imposes a lower bound on the de-biased B-scan, which maintains a reasonable dynamic range after converting to dB. Recall from §III-A that de-biasing the B-scans is a necessary first step in isolating the parameters of the confocal function. Once debiased, reduce the effects of speckle with a digital filter [24]. For the results presented in this paper, we used a separable Gaussian filter with a standard deviation of 0.7 pixels (chosen to suppress high frequency noise while maintaining structure). After speckle has been reduced, account for fall-off by dividing the data by the fall-off function. (It may not be necessary to account for fall-off; refer to Appendix E for details. Fall-off was not taken into account for the results presented in this paper.) Finally, convert the results to decibels.

Step 2 (Filter Converted B-Scans): The confocal function is known to vary slowly across an A-scan. High spatial frequencies present in the imagery, either due to structure or noise, corrupt the calculation of the confocal function parameters. To reduce this corruption, filter the de-biased B-scans (in dB) with a low-pass filter (e.g., a Gaussian filter) to obtain the de-biased, filtered images $\hat{\boldsymbol{I}}_{\mathbf{1}}^{(\text{dB})}$ and $\hat{\boldsymbol{I}}_{\mathbf{2}}^{(\text{dB})}$. For the results presented in this paper, we used a separable Gaussian filter with a standard deviation of 9 pixels in each dimension (the results are not sensitive to this parameter); this value creates a broad filter that further reduces speckle and eliminates some structure but permits the confocal function to pass without much distortion. Filtration was performed in the spatial-frequency domain.

Step 3 (Align Filtered B-Scans): Identify peaks in $\hat{\boldsymbol{I}}_{\mathbf{1}}^{(\text{dB})}$, defined as local maxima in the sum of the vertical and horizontal forward differences[4]: $(D_z + D_x)\,\hat{\boldsymbol{I}}_{\mathbf{1}}^{(\text{dB})}$. Peaks were chosen because they are present in virtually all data, which makes this method generally applicable. The number of peaks identified is a user-defined parameter. For the results presented in this manuscript, 100 peaks were detected in $\hat{\boldsymbol{I}}_{\mathbf{1}}^{(\text{dB})}$; peaks were not permitted to be within 20 pixels of each other. Track the peaks into $\hat{\boldsymbol{I}}_{\mathbf{2}}^{(\text{dB})}$ using normalized cross correlation [25]. Determine the alignment parameters (Δx, Δz, and ζ) from matched points using the Random Sample Consensus (RANSAC) algorithm [26], which is robust against erroneous matches. For the results presented in this manuscript, approximately 20% of the peaks were retained as valid matches; given the three degrees of freedom of the alignment (a shear and a translation), the number of valid matches was more than sufficient. Once the translation and shear parameters have been estimated, transform $\hat{\boldsymbol{I}}_{\mathbf{2}}^{(\text{dB})}$ so that it is aligned with $\hat{\boldsymbol{I}}_{\mathbf{1}}^{(\text{dB})}$. Note that several values of the transformed $\hat{\boldsymbol{I}}_{\mathbf{2}}^{(\text{dB})}$ do not overlap values in $\hat{\boldsymbol{I}}_{\mathbf{1}}^{(\text{dB})}$; only those pixels that are imaged in both B-scans are included when evaluating (6) in step 4. This step is a completely automatic algorithm for aligning B-scans and identifying the overlapping region.

Step 4 (Determine the Parameters of the Confocal Function):

Set the weights of the norm in (6) using $w = \max\left(0, \min\left(\hat{\boldsymbol{I}}_{\mathbf{1}}^{(dB)}, \hat{\boldsymbol{I}}_{\mathbf{2}}^{(dB)}\right)\right)$.

Due to the high intensity of the pixels near the surface resulting from a high index mismatch, these pixels alter the optimal point of the weighted norm significantly. Therefore, any misregistration at the surface reduces the quality of the resulting estimate. To correct for this, set the weights of the norm to 0 for any points near the surface and above. The surface locations of each A-scan are found independently, similarly to the method presented in [12]. Set t_l and t_h to the median values of the lowest 10% and highest 90% of pixel intensities, respectively. Consider the top-most point of each A-scan whose intensity value exceeds $t = \text{mean}(t_l, t_h)$ to be the surface. Create a mask $X \in \mathbb{R}^{M\times N}$ so that $X_{ij} = 0$ if the pixel is above the surface and $X_{ij} = 1$ if the pixel is below the surface. Apply an erosion operation to the mask X to eliminate points near the surface where the difference in the index of refraction may be high. Note that this method of surface extraction may not be suitable for all samples (e.g., samples with fur or a highly reflective surface), in which case a more sophisticated technique may be required [27].

Set the weights of the norm so that $w := X \odot w$, where $\odot$ denotes the Hadamard product. With these weights, determine the optimal values of z_0 and z_R by minimizing (6). For the results of this paper, we used the `fmincon` implementation of interior point methods in MATLAB for the optimization.

Step 5 (Estimate the Attenuation Coefficients): To determine the attenuation coefficients, process $\hat{\boldsymbol{I}}_{\mathbf{1}}$ with DRC as described

[4]A forward difference is a first order approximation to the derivative; it is defined as $Df(t) = f(t+1) - f(t)$.

in Appendix B. Note that for any other B-scans captured with the same system configuration (i.e., B-scans collected with the same z_0 and z_R, e.g. $\hat{\boldsymbol{I}}_2$), only this step must be repeated to quantify the attenuation coefficients.

IV. Experimental Design

A. Phantom Experiment

To assess the effectiveness of autoConfocal+DRC, the algorithm was run on OCT imagery of a five-layer phantom made from titanium dioxide (TiO_2) and poly(dimethylsiloxane) (PDMS). The attenuation coefficients of each layer were controlled as detailed in Appendix D. Various lateral translations and rotations between the two B-scans were tested to show the effect of these parameters on the performance of autoConfocal. Each layer of the phantom was made by dispersing TiO_2 in PDMS [28], [29], and the attenuation of each layer was controlled by adjusting the concentration of TiO_2. The topology of the second layer was created by placing pieces of wire into the PDMS prior to curing. The wire pieces were subsequently removed and the top layer of PDMS was used to fill in the holes remaining from the wire and create a final layer. The shape of the phantom (in particular, the indentations in the second layer) was chosen to provide edges that would generate peaks from which two B-scans could be aligned. In this way, the phantom is representative of many biological samples, which are rarely uniform in the lateral direction.

OCT measurements of the phantom were collected with a commercial SD-OCT system ($\lambda_0 = 1325$ nm, TELESTO, ThorLabs). A lateral scanning lens (LSM03, ThorLabs) with a Rayleigh range of 105.91 μm (provided by the manufacturer) was installed, which yielded a lateral resolution of 15 μm and an axial resolution in air of 7.5 μm. Raw interferograms were collected without averaging, and B-scans were obtained through processing with a custom MATLAB script. The imaging depth and lateral range captured were both 2.57 mm; each B-scan was stored in a 512×512 image. The phantom was imaged through a layer of ultrasound gel to reduce surface reflections caused by a mismatch in the refractive indices.

B. Ex-Vivo Tissue Experiment

To show the performance of autoConfocal+DRC on actual tissue, it was run on imagery of an *ex-vivo* rabbit eye, which was harvested from a healthy rabbit euthanized as part of an unrelated study. The sclera of the eye was imaged from the outside through a portion of fatty tissue. The measurements of the rabbit eye were collected using the same SD-OCT system as the phantom experiments (TELESTO, ThorLabs).

C. Clinical Experiment

To demonstrate the ability of autoconfocal+DRC to perform well on a clinical OCT system, it was run on imagery of the *in-vivo* normal human retina of the author (TL). These measurements were collected with a commercial SD-OCT system ($\lambda_0 = 840$ nm, Cirrus HD-OCT model 5000, Carl Zeiss Meditec) with a lateral and axial resolution in tissue of 15 μm and 5 μm, respectively, and a Rayleigh range of 0.21 mm. Eye tracking was used to center both B-scans on the foveal pit.

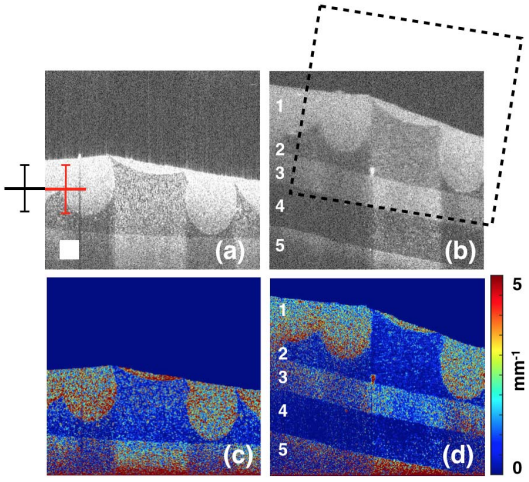

Fig. 2. Results shown of a five-layered phantom. (a) and (b) are the input B-scans (in dB). The white square in (a) represents 0.25×0.25 mm^2. The black line and bars in (a) indicate the true $z_0 \pm z_R$; the red line and bars indicate the estimated $z_0 \pm z_R$ using autoConfocal. The black dashed box indicates the outline of (a) after alignment with (b). In the resulting attenuation coefficient images (c) and (d), the alternating structure of attenuation in the layers is clearly visible. Note that the scale bar of (d) shows the values of attenuation coefficients in (c) and (d).

V. Results

A. Phantom Experiment

Fig. 2 shows the result of autoConfocal+DRC on different B-scans of the phantom that are related by a lateral translation of approximately 0.25 mm and a rotation of approximately 10 degrees. Figures 2 (a) and (b) show the two input B-scans (in dB). The horizontal black line indicates the position of the focal plane location at 1.6 mm, as determined visually by manually translating the sample in and out of the focal plane and identifying the plane of maximum brightness (which has an accuracy of approximately 0.1 mm). The bars on the black line represent $\pm z_R = 0.30$ mm, the apparent Rayleigh range of the objective reported by the manufacturer (after accounting for the refractive index of the phantom and setting $\alpha = 2$ for a diffuse scattering medium). The red line and bars indicate the values of the focal plane and apparent Rayleigh range (1.6 mm and 0.31 mm, respectively) determined by autoConfocal. Note that the differences in these values are within the tolerance required for accurate quantification of the attenuation coefficient by DRC (100% and 125% of the Rayleigh range for the focal plane position and Rayleigh range, respectively, as detailed in Appendix C). Figures 2 (c) and (d) show the attenuation coefficient images of (a) and (b), respectively, calculated by DRC; the alternating structure of attenuation in the layers is clearly observed.

Table I shows how the mean estimate of each layer of the phantom in Fig. 2 (d) compares to the intended attenuation coefficient of each layer. The difference in estimated versus intended attenuation coefficient of layers 1 and 2 is within the error of measured TiO_2 when making the phantom (based on the accuracy of the scale used to weigh the TiO_2). The error is small until the depth is large; this is expected since the SNR decreases with depth. The nonuniformity and the large error of the fifth layer is due to the low SNR deep in the sample.

TABLE I
MEAN ATTENUATION COEFFICIENTS FOR EACH LAYER OF FIG. 2(d) COMPARED TO THE INTENDED VALUES

Layer	1	2	3	4	5
Intended (mm^{-1})	2.6	0.4	1.8	0.4	8.0
Estimated (mm^{-1})	2.9	0.5	1.8	0.2	5.8
Error (mm^{-1})	0.3	0.1	0.0	-0.2	-2.2

Due to the presence of aliasing (and corresponding intensity values that are higher than expected), DRC under-estimates the attenuation coefficients deeper in the sample.

Results showing the uncertainty of the estimated confocal function parameters and in the estimated attenuation coefficients from the phantom experiments are presented in Appendix D-A.

B. Ex-Vivo Tissue Experiment

To demonstrate the utility of autoConfocal+DRC on actual tissue, the algorithm was run on imagery of *ex-vivo* rabbit tissue. Figures 3 (a) and (b) show two B-scans of a rabbit eye. Note that the fatty tissue and sclera are separated by a layer with seemingly low attenuation (i.e., dark in the intensity image). The white line and bars indicate the values of the focal plane and apparent Rayleigh range estimated by autoConfocal (0.77 mm and 0.20 mm, respectively). These values are within the tolerable error from the actual focal plane location (0.75 mm) and apparent Rayleigh range (0.29 mm), indicated by the horizontal black line and corresponding bars. Similar to the phantom data, the assumed focal plane location was determined visually and the apparent Rayleigh range was calculated using (3) from the Rayleigh range specified by the manufacturer (with α set to 2 since the tissue is a diffuse scattering medium, and an index of refraction of 1.37). Figures 3 (c) and (d) show the attenuation coefficients estimated by DRC. Notably, the areas indicated with arrows in the attenuation image (Fig. 3 (d)) show higher contrast than their counterparts in the B-scan, which demonstrates the utility of autoConfocal paired with DRC. Using the method of [30], the attenuation coefficient of the fatty tissue in the boxed region of Fig. 3 (c) was determined to be 5.8 mm^{-1}. The mean of the attenuation coefficient values determined by autoConfocal+DRC was 5.4 mm^{-1}, which is similar. The method of [30] assumes that the sample has a constant attenuation; the difference in the two estimates reflects how much this assumption is violated in the hand-selected region.

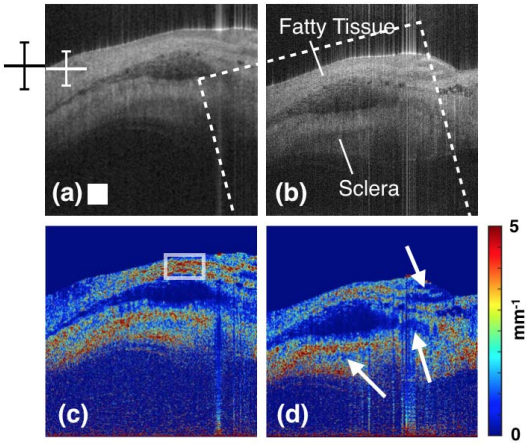

Fig. 3. Results shown of an *ex-vivo* rabbit eye using data collected with a TELESTO. (a) and (b) are the input B-scans (in dB), and (c) and (d) are the resulting attenuation coefficient images. The dashed box indicates the outline of (a) after alignment with (b). In (d), the arrows indicate areas of increased contrast over the B-scans. The average attenuation coefficient in the box in (c) is consistent with results using previously reported techniques. The white square in (a) represents 0.25×0.25 mm^2. Note that the scale bar shows the values of attenuation coefficients in (c) and (d).

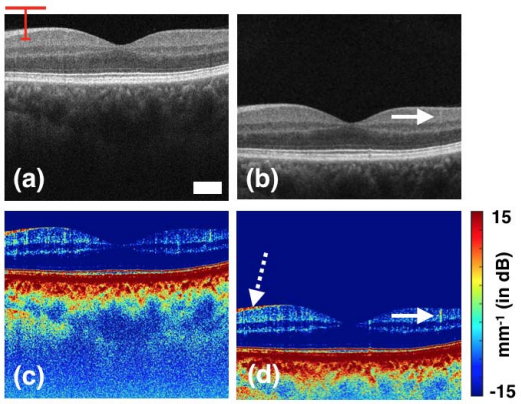

Fig. 4. Results shown of a human eye using data from a Zeiss Cirrus 5000 HD-OCT. Figs. (a) and (b) are the input B-scans (in dB), and (c) and (d) are the resulting attenuation coefficient images. The red line and bar in (a) indicate the estimated z_0 and z_R using autoConfocal, respectively. The white square in (a) represents 0.25×0.25 mm^2. Note that the scale bars show the values of attenuation coefficients in (c) and (d). The dashed arrow in (d) points to the nerve fiber layer of the retina. The arrow in (b) points to a shadow that results from a superficial retinal blood vessel. The arrow in (d) points to the corresponding streak in the attenuation coefficient results.

C. Clinical Experiment

We further show the utility of autoConfocal+DRC using data collected from an *in-vivo* human retina using a Cirrus HD-OCT system. The input B-scans of human retina in dB are shown in Figs. 4 (a) and (b), while (c) and (d) show the attenuation coefficient image produced with Alg. 1. Eye tracking was used to center both B-scans on the foveal pit, a common practice in ophthalmic evaluations of the retina.

The red line and bar in Fig. 4 (a) indicate the values of the focal plane and apparent Rayleigh range estimated by autoConfocal (−0.09 and 0.64 mm, respectively). The apparent Rayleigh range was within the tolerable error from the actual apparent Rayleigh range of the system, which was determined using (3) and by equating the lateral resolution with the $1/e^2$ spot size. The value of α was set to 2 and the index of refraction was set to 1.37. The mean attenuation coefficient of the nerve fiber layer (indicated with the dashed arrow in Fig. 4 (d)) was measured to be 3.8 mm^{-1} with a standard deviation of 2.5 mm^{-1}. This is consistent with the measured attenuation coefficient of the nerve fiber layer in the nasal region of the retina reported in [5] (3.60 ± 0.53), indicating that autoConfocal+DRC is capable of producing accurate attenuation coefficient estimates with clinical data

where the focal plane location and apparent Rayleigh range are inaccessible to the user. The mean attenuation coefficient of the nerve fiber layer in Fig. 4 (c) was measured to be 3.3 mm^{-1} with a standard deviation of 2.2 mm^{-1}, which demonstrates consistency of the autoconfocal+DRC algorithm. The streak in Fig. 4 (b), indicated by an arrow, represents shadowing from a superficial retinal blood vessel. The resulting low SNR in this area creates a corresponding streak in the attenuation coefficient image (Fig. 4 (d)), again indicated by an arrow.

Fig. 4 represents the first time that the attenuation coefficients of each layer of the retina were estimated when the focal plane was close to the imaged sample. The attenuation coefficient of the nerve fiber layer has already been implicated in glaucoma diagnosis and monitoring [5]; we are hopeful that the newly provided access to the attenuation coefficients of additional layers will aid in the diagnosis of other conditions.

D. Error Analysis

Recall that the DRC algorithm assumes negligible absorption. Results in [31] ans [32] show the ratio of absorption to scattering in human sclera and bovine retina is approximately $5-10\%$. This suggests (based on §III-B) that the *ex-vivo* and *in-vivo* attenuation coefficient estimates of this study (rabbit sclera imaged at 1325 nm and human retina imaged at 840 nm) have an error of $5-10\%$. However, further study would be needed to confirm this because the tissue types of this study are not identical to those reported (i.e., human vs. rabbit sclera and human vs. bovine retina). Results presented in [33]–[36] show the ratio of absorption to scattering for many other biological tissues (e.g., dermis, epidermis, brain, breast, bladder, bowel) is also approximately $5-10\%$. Thus, $5-10\%$ is a plausible upper bound on the error.[5] Note that this does not hold for biological media that is highly absorbing (e.g., blood); therefore, DRC is not an appropriate algorithm for tissue in an A-scan containing highly absorbing media (i.e., quantification of tissue above or below blood vessels is inaccurate).

Figs. 4(c) and (d) show high spatial variation of the attenuation coefficient within layers of the retina. The total error will be the sum of the numerical error and the error due to absorption. Both PDMS and TiO_2 have negligible absorption in the wavelength range of the TELESTO. Therefore, the error in the phantom is strictly due to numerical issues. From the results presented in Appendix D, the error of the phantom is less than 7% (a maximum standard deviation of 0.2 mm^{-1} with a maximum attenuation of approximately 2.9 mm^{-1}). As discussed, the error due to absorption is likely between $5-10\%$. Thus, the sum of the two errors is less than 17%. The standard deviation of the measured attenuation coefficients for the *in-vivo* retinal data (2.2 mm^{-1}) is higher than this value; we hypothesize that these variations are likely due to anatomy (though some of these variations are due to speckle that was not filtered out). In the future, it may be valuable to determine the potential diagnostic value of spatial variation within such a layer.

[5]If the attenuation due to absorption were non-negligible but proportional to the attenuation due to scattering then the error would be deterministic and could be taken into account. However, there is no reason to believe that this would be the case for biological tissue.

VI. Conclusion

We have described a method to automatically determine the confocal function parameters of an OCT system from two B-scans when the focal plane is either in the sample or close to the surface. For clinical applications, these are the preferred cases due to the high SNR of the imagery. The confocal function parameters were then successfully used to calculate the attenuation coefficient via the DRC algorithm. In several cases shown, the contrast achieved with the attenuation coefficient, which represents the underlying physiology, cannot be seen in the original B-scans. This will allow for attenuation coefficient measurements on OCT systems without the need for a manual calibration process or access to separate samples.

When the focal plane is distant from the surface of the sample (and the confocal function is nearly constant), autoConfocal becomes inaccurate because the intensity difference in the two B-scans due to the confocal function is very small. That error propagates through DRC and yields inaccurate estimates of the attenuation coefficients. If it were known *a priori* whether or not the focal plane is near the surface of the sample, then one could use the DR technique when the focal plane is high above the surface and autoConfocal+DRC when the focal plane is close to or within the sample.

The algorithm presented in this paper assumes that the amount of backscattered light is a fixed fraction of the total light scattered as described in (1). Recent work by Almasian et al. shows that the amount of backscattered light is a function of particle size when the optical size (a dimensionless number defined as the particle diameter times the center angular wave number) is less than 5 [37]. If the distribution of particle sizes in each voxel was known *a priori*, then this assumption could be taken into account, but a method for estimating particle sizes from the OCT signal has yet to be discovered.

In this paper, we also assumed that the two B-scans processed by autoConfocal are related by a rotation and a translation. This is appropriate for ophthalmic data where feature tracking can be used to ensure that the data remains in-plane (as was done with the results shown in Fig. 4); however, this assumption may not be appropriate for other applications (e.g., bladder or skin imaging). For these applications, it may be necessary to implement a version of the proposed method on three-dimensional data, which we leave for future work.

Acknowledgments

The authors would like to thank Yamil Saenz and Christopher Sandino for providing us with a euthanized rabbit. The authors would also like to thank Mary Durbin and Tilman Schmoll from Zeiss for helping us interpret the clinical data. Finally, the authors would like to thank the reviewers of this document for their many insightful comments.

References

[1] R. J. Hodgson, P. O'Connor, and R. Moots, "MRI of rheumatoid arthritis—Image quantitation for the assessment of disease activity, progression and response to therapy," *Rheumatology*, vol. 47, no. 1, pp. 13–21, 2008.

[2] W. Li, A. F. van der Steen, C. T. Lancée, I. Céspedes, and N. Bom, "Blood flow imaging and volume flow quantitation with intravascular ultrasound," *Ultrasound Med. Biol.*, vol. 24, no. 2, pp. 203–214, 1998.

[3] R. S. Shamberger, R. S. Holzman, N. T. Griscom, N. J. Tarbell, and H. J. Weinstein, "CT quantitation of tracheal cross-sectional area as a guide to the surgical and anesthetic management of children with anterior mediastinal masses," *J. Pediatric Surg.*, vol. 26, no. 2, pp. 138–142, 1991.

[4] S. Liu *et al.*, "Tissue characterization with depth-resolved attenuation coefficient and backscatter term in intravascular optical coherence tomography images," *J. Biomed. Opt.*, vol. 22, no. 9, p. 096004, 2017.

[5] J. van der Schoot, K. A. Vermeer, J. F. de Boer, and H. G. Lemij, "The effect of glaucoma on the optical attenuation coefficient of the retinal nerve fiber layer in spectral domain optical coherence tomography images," *Invest. Ophthalmol. Vis. Sci.*, vol. 53, no. 4, pp. 2424–2430, 2012.

[6] K. Barwari, D. M. de Bruin, D. J. Faber, T. G. van Leeuwen, J. J. de la Rosette, and M. P. Laguna, "Differentiation between normal renal tissue and renal tumours using functional optical coherence tomography: A phase I *in vivo* human study," *BJU Int.*, vol. 110, no. 8b, pp. E415–E420, 2012.

[7] E. C. Cauberg *et al.*, "Quantitative measurement of attenuation coefficients of bladder biopsies using optical coherence tomography for grading urothelial carcinoma of the bladder," *J. Biomed. Opt.*, vol. 15, no. 6, p. 066013, 2010.

[8] W. Yuan, C. Kut, W. Liang, and X. Li, "Robust and fast characterization of OCT-based optical attenuation using a novel frequency-domain algorithm for brain cancer detection," *Sci. Rep.*, vol. 7, Mar. 2017, Art. no. 44909.

[9] C. Kut *et al.*, "Detection of human brain cancer infiltration *ex vivo* and *in vivo* using quantitative optical coherence tomography," *Sci. Transl. Med.*, vol. 7, no. 292, p. 292ra100, 2015.

[10] K. A. Vermeer, J. Mo, J. J. A. Weda, H. G. Lemij, and J. F. de Boer, "Depth-resolved model-based reconstruction of attenuation coefficients in optical coherence tomography," *Biomed. Opt. Express*, vol. 5, no. 1, pp. 322–337, 2014.

[11] T. G. V. Leeuwen, D. J. Faber, and M. C. Aalders, "Measurement of the axial point spread function in scattering media using single-mode fiber-based optical coherence tomography," *IEEE J. Sel. Topics Quantum Electron.*, vol. 9, no. 2, pp. 227–233, Mar. 2003.

[12] G. T. Smith *et al.*, "Automated, depth-resolved estimation of the attenuation coefficient from optical coherence tomography data," *IEEE Trans. Med. Imag.*, vol. 34, no. 12, pp. 2592–2602, Dec. 2015.

[13] M. Almasian, N. Bosschaart, T. G. van Leeuwen, and D. J. Faber, "Validation of quantitative attenuation and backscattering coefficient measurements by optical coherence tomography in the concentration-dependent and multiple scattering regime," *J. Biomed. Opt.*, vol. 20, no. 12, p. 121314, 2015.

[14] J. Schmitt, D. Kolstad, and C. Petersen, "Intravascular optical coherence tomography opens a window onto coronary artery disease," *Opt. Photon. News*, vol. 15, no. 2, pp. 20–25, 2004.

[15] T. Wang *et al.*, "Intravascular optical coherence tomography imaging at 3200 frames per second," *Opt. Lett.*, vol. 38, no. 10, pp. 1715–1717, 2013.

[16] M. J. Manyak *et al.*, "Evaluation of superficial bladder transitional-cell carcinoma by optical coherence tomography," *J. Endourol.*, vol. 19, no. 5, pp. 570–574, 2005.

[17] K. L. Lurie and A. K. Ellerbee, "Volumetric mosaicing for optical coherence tomography for large area bladder wall visualization," *Proc. SPIE*, vol. 8926, p. 89261P, Mar. 2014.

[18] N. Dwork, G. T. Smith, J. M. Pauly, and A. K. E. Bowden, "Automated estimation of OCT confocal function parameters from two B-scans," in *Proc. Conf. Lasers Electro-Opt.*, 2016, pp. 1–2, Paper AW1O-4.

[19] S. H. Yun, G. J. Tearney, B. E. Bouma, B. H. Park, and J. F. de Boer, "High-speed spectral-domain optical coherence tomography at 1.3 μm wavelength," *Opt. Express*, vol. 11, no. 26, pp. 3598–3604, 2003.

[20] M. Hagen-Eggert, P. Koch, and G. Hüttmann, "Analysis of the signal fall-off in spectral domain optical coherence tomography systems," *Proc. SPIE*, vol. 8213, p. 82131K, Feb. 2012.

[21] A. W. Paeth, "A fast algorithm for general raster rotation," *Graph. Interface*, vol. 86, no. 5, pp. 77–81, 1986.

[22] S. Boyd and L. Vandenberghe, *Convex Optimization*. Cambridge, U.K.: Cambridge Univ. Press, 2004.

[23] R. Wessels *et al.*, "Learning curve and interobserver variance in quantification of the optical coherence tomography attenuation coefficient," *J. Biomed. Opt.*, vol. 20, no. 12, p. 121313, 2015.

[24] A. Ozcan, A. Bilenca, A. E. Desjardins, B. E. Bouma, and G. J. Tearney, "Speckle reduction in optical coherence tomography images using digital filtering," *J. Opt. Soc. Amer. A, Opt. Image Sci.*, vol. 24, no. 7, pp. 1901–1910, 2007.

[25] J. P. Lewis, "Fast normalized cross-correlation," *Vis. Interface*, vol. 10, no. 1, pp. 120–123, May 1995.

[26] R. Hartley and A. Zisserman, *Multiple View Geometry in Computer Vision*, 2nd ed. Cambridge, U.K.: Cambridge Univ. Press, 2003.

[27] L. Duan, T. Marvdashti, A. Lee, J. Y. Tang, and A. K. Ellerbee, "Automated identification of basal cell carcinoma by polarization-sensitive optical coherence tomography," *Biomed. Opt. Express*, vol. 5, no. 10, pp. 3717–3729, 2014.

[28] G. T. Smith, K. L. Lurie, S. A. Khan, J. C. Liao, and A. K. Ellerbee, "Multilayered disease-mimicking bladder phantom with realistic surface topology for optical coherence tomography," *Proc. SPIE*, vol. 8945, p. 89450E, Mar. 2014.

[29] K. L. Lurie, G. T. Smith, S. A. Khan, J. C. Liao, and A. K. Ellerbee, "Three-dimensional, distendable bladder phantom for optical coherence tomography and white light cystoscopy," *J. Biomed. Opt.*, vol. 19, no. 3, p. 036009, 2014.

[30] D. J. Faber, F. J. van der Meer, M. C. G. Aalders, and T. G. van Leeuwen, "Quantitative measurement of attenuation coefficients of weakly scattering media using optical coherence tomography," *Opt. Express*, vol. 12, no. 19, pp. 4353–4365, 2004.

[31] A. N. Bashkatov, E. A. Genina, V. I. Kochubey, and V. V. Tuchin, "Optical properties of human sclera in spectral range 370–2500 nm," *Opt. Spectrosc.*, vol. 109, no. 2, pp. 197–204, 2010.

[32] B. G. Yust, L. C. Mimun, and D. K. Sardar, "Optical absorption and scattering of bovine cornea, lens, and retina in the near-infrared region," *Lasers Med. Sci.*, vol. 27, no. 2, pp. 413–422, 2012.

[33] E. V. Salomatina, B. Jiang, J. Novak, and A. N. Yaroslavsky, "Optical properties of normal and cancerous human skin in the visible and near-infrared spectral range," *J. Biomed. Opt.*, vol. 11, no. 6, p. 064026, 2006.

[34] A. N. Yaroslavsky, P. C. Schulze, I. V. Yaroslavsky, R. Schober, F. Ulrich, and H. J. Schwarzmaier, "Optical properties of selected native and coagulated human brain tissues *in vitro* in the visible and near infrared spectral range," *Phys. Med. Biol.*, vol. 47, no. 12, p. 2059, 2002.

[35] A. E. Cerussi *et al.*, "Sources of absorption and scattering contrast for near-infrared optical mammography," *Acad. Radiol.*, vol. 8, no. 3, pp. 211–218, 2001.

[36] J. L. Sandell and T. C. Zhu, "A review of *in-vivo* optical properties of human tissues and its impact on PDT," *J. Biophoton.*, vol. 4, nos. 11–12, pp. 773–787, 2011.

[37] M. Almasian, T. G. Leeuwen, and D. J. Faber, "OCT amplitude and speckle statistics of discrete random media," *Sci. Rep.*, vol. 7, no. 1, 2017, Art. no. 14873.